





Article

Synthesis and Photocatalytic Properties of Manganese-Substituted Layered Perovskite-like Titanates $A'_{2}La_{2}Mn_{x}Ti_{3-x}O_{10}$ ($A' = Na, H$)

Sergei A. Kurnosenko ¹, Anastasiya I. Ustinova ¹, Iana A. Minich ¹, Vladimir V. Voytovich ¹, Oleg I. Silyukov ^{1,*}, Dmitrii V. Pankin ², Olga V. Volina ³, Alina V. Kulagina ¹ and Irina A. Zvereva ¹

¹ Department of Chemical Thermodynamics and Kinetics, Institute of Chemistry, Saint Petersburg State University, Saint Petersburg 199034, Russia; s.kurnosenko@spbu.ru (S.A.K.); st097834@student.spbu.ru (A.I.U.); yana.minich@spbu.ru (I.A.M.); st062003@student.spbu.ru (V.V.V.); st094540@student.spbu.ru (A.V.K.); irina.zvereva@spbu.ru (I.A.Z.)

² Center for Optical and Laser Materials Research, Research Park of Saint Petersburg State University, Saint Petersburg 199034, Russia; dmitrii-pankin@spbu.ru

³ Center for Chemical Analysis and Materials Research, Research Park of Saint Petersburg State University, Saint Petersburg 199034, Russia; o.volina@spbu.ru

* Correspondence: oleg.silyukov@spbu.ru

Abstract: The search for effective and reliable methods of photosensitization of oxide-based semiconductor materials is of great significance for their use in photocatalytic reactions of hydrogen production and environmental remediation under natural sunlight. The present study is focused on partial substitution of titanium with manganese in the structure of layered perovskite-like titanate $Na_{2}La_{2}Ti_{3}O_{10}$, which was employed to yield a series of photocatalytically active materials, $Na_{2}La_{2}Mn_{x}Ti_{3-x}O_{10}$ ($x = 0.002-1.0$), as well as their protonated forms $H_{2}La_{2}Mn_{x}Ti_{3-x}O_{10}$ and nanosheets. It was established that the manganese cations Mn^{4+} are embedded in the middle sublayer of oxygen octahedra in the perovskite slabs $La_{2}Mn_{x}Ti_{3-x}O_{10}^{2-}$ and that the maximum achievable manganese content x in the products is ≈ 0.9 . The partial cationic substitution in the perovskite sublattice led to a pronounced contraction of the optical band gap from 3.20 to 1.35 eV (depending on x) and, therefore, allowed the corresponding photocatalysts to utilize not only ultraviolet, but also visible and near-infrared light with wavelengths up to ≈ 920 nm. The materials obtained were tested as photocatalysts of hydrogen evolution from aqueous methanol, and the greatest activity in this reaction was demonstrated by the samples with low manganese contents ($x = 0.002-0.01$). However, the materials with greater substitution degrees may be of high interest for use in other photocatalytic processes and, especially, in thermophotocatalysis due to their improved ability to absorb the near-infrared part of solar radiation.

Keywords: layered perovskite; photosensitization; cationic substitution; protonation; exfoliation; nanosheets; photocatalysis; hydrogen



Academic Editor: Tarek Abdel-Fattah

Received: 30 March 2025

Revised: 5 May 2025

Accepted: 9 May 2025

Published: 12 May 2025

Citation: Kurnosenko, S.A.; Ustinova, A.I.; minich, I.A.; Voytovich, V.V.; Silyukov, O.I.; Pankin, D.V.; Volina, O.V.; Kulagina, A.V.; Zvereva, I.A. Synthesis and Photocatalytic Properties of Manganese-Substituted Layered Perovskite-like Titanates $A'_{2}La_{2}Mn_{x}Ti_{3-x}O_{10}$ ($A' = Na, H$). *Solids* **2025**, *6*, 23. <https://doi.org/10.3390/solids6020023>

Copyright: © 2025 by the authors. Licensee MDPI, Basel, Switzerland. This article is an open access article distributed under the terms and conditions of the Creative Commons Attribution (CC BY) license (<https://creativecommons.org/licenses/by/4.0/>).

1. Introduction

For a long time, among other classes of ceramic materials, considerable attention of researchers has been paid to ion-exchangeable layered perovskite-like oxides. The latter represent crystalline solids with a block structure that consists of negatively charged fused plates with a thickness of n perovskite octahedra separated at the corners, regularly alternating with interlayer spaces populated by alkali cations [1]. Valuable physicochemical properties of these oxides are associated with the unique perovskite structure, as well as the

pronounced activity of the interlayer space in ion exchange and intercalation reactions [2,3]. Some representatives of layered perovskite-like oxides are known to be promising catalysts and photocatalysts [4–10], ionic conductors [11–15], ferroelectric [16], piezoelectric [17] and luminescent [18] materials, components for creating chemical sensors [19], fuel cells and photovoltaic devices [20,21]. In addition, of special interest are organically modified forms of layered perovskite-like oxides [22–30] that have proven to be highly efficient photocatalysts of hydrogen generation [31–33] and convenient precursors for producing perovskite nanosheets [34]. Among other factors, unique photocatalytic properties of these materials are associated with their chemically active interlayer space that is suggested to function as a special reaction zone along with the external surface of the crystals [5].

Another feature of layered perovskite-like oxides is that their photocatalytic properties can be further improved by partial ionic substitution in the perovskite sublattice with only minor structural changes. In addition to reducing bandgap energy (for exhibiting photocatalytic activity in the visible spectrum region), in some cases, the crystal deformation caused by the ionic substitution can provide a trap for photogenerated electrons and holes, thereby facilitating their spatial separation and enhancing the photocatalytic performance. A similar approach has previously been studied using the example of titanium dioxide and some complex oxides [35–37]. Due to the structural features of the perovskite block of layered perovskite-like oxides, substitution can occur at several positions: substitution of a cation in a metal–oxygen octahedron (at the position B), substitution of a cation located between several metal–oxygen octahedra (at the position A), and anionic substitution of oxygen by another anion. Partial ionic substitution in the perovskite sublattice allows not only expanding the light absorption range but also preserving the interlayer space for further topochemical manipulations, in particular ion exchange, intercalation and organic modification. However, to date, most studies are devoted to anionic substitution, in particular, the replacement of oxygen with nitrogen (nitriding), and, less often, with other anions by post-treatment [38–46].

The starting object of this investigation, $\text{Na}_2\text{La}_2\text{Ti}_3\text{O}_{10}$, is a representative of layered titanates $\text{A}'_2\text{Ln}_2\text{Ti}_3\text{O}_{10}$ belonging to the so-called Ruddlesden–Popper phases, described by a general formula $\text{A}'_2[\text{A}_{n-1}\text{B}_n\text{O}_{3n+1}]$. The structure of the titanates $\text{A}'_2\text{Ln}_2\text{Ti}_3\text{O}_{10}$ comprises a regular alternation of perovskite blocks with a thickness of $n = 3$ titanium–oxygen octahedra TiO_6 , with interlayer spaces populated by alkali cations A' [47]. These compounds and composite materials based on them have already proven to be highly efficient photocatalysts for hydrogen production and water purification [48–54]. However, a relatively wide band gap of the unmodified titanates, exceeding 3 eV, only allows utilization in photocatalysis of ultraviolet radiation, which accounts for only a few percent of the solar spectrum. In view of this, the wide practical application of these materials requires their photosensitization, one of the methods of which is partial ionic substitution in the perovskite blocks.

For layered Ruddlesden–Popper titanates $\text{A}'_2\text{Ln}_2\text{Ti}_3\text{O}_{10}$, there is a noticeably large number of studies on cationic substitution in the perovskite sublattice using V, Cr, Fe, Ni, Zn, Nb, Sn, W and other elements [55–60] implemented by direct synthesis of the corresponding solid solutions. Unfortunately, a significant drawback of most studies devoted to cation substitution is the insufficient characterization of the obtained materials from a chemical and structural point of view. The authors usually indicate the degree of substitution «by loading» of the reactants and do not confirm the actual ratio of elements in the products. However, in a number of cases, the cation substitution proved its effectiveness in light of increasing photocatalytic activity of layered titanates in the visible spectrum range. For instance, the authors of the study [59] partially substituted Ti in the $\text{K}_2\text{La}_2\text{Ti}_3\text{O}_{10}$ structure with Fe, Ni and W, which led to the bathochromic shift of the long-wave absorption edge and appearance of photocatalytic activity in the reaction of hydrogen generation from a

Na₂S/Na₂SO₃ aqueous solution under visible light. It was also shown that the most active photocatalysts are those with small substitution degrees ($x \leq 0.2$), although the higher degrees provided a greater long-wave shift of the absorption maximum. The preparation of solid solutions of layered titanates with manganese was also previously considered in the literature [61]. Since the mentioned paper was focused on magnetic properties of the prepared materials, it did not include evaluating light absorption characteristics and photocatalytic properties. At the same time, the authors successfully obtained several series of the titanates Na₂Ln₂Mn_xTi_{3-x}O₁₀ (Ln = Sm, Eu, Gd and Dy) with a wide range of substitution degrees ($0 < x \leq 1.0$) and investigated the correlation between the specific lanthanide and achievable substitution maximum. Additionally, the authors attempted a synthesis of similar manganese-containing titanates with Ln = La and claimed that the highest feasible substitution degree is only $x = 0.8$, while the attempts to obtain compounds with greater manganese contents led to the formation of impurity phases.

Meanwhile, in addition to magnetic properties, the manganese-substituted titanates and their derivatives can potentially be used as photocatalysts that are active in the visible region of the spectrum. In view of the above, the present study is devoted to the synthesis of layered perovskite-like titanates, Na₂La₂Mn_xTi_{3-x}O₁₀, with a variable degree of substitution of titanium for manganese ($0 < x \leq 1.0$). Special attention is paid to confirmation of the structure and factual composition of the products, as well as photophysical characteristics and photocatalytic activity of their protonated forms and nanosheets.

2. Materials and Methods

2.1. Synthesis of Alkaline Titanates Na₂La₂Mn_xTi_{3-x}O₁₀ ($x = 0, 0.002, 0.005, 0.025, 0.05, 0.1, 0.3, 0.5, 0.7, 0.9, 1.0$)

The alkaline layered perovskite-like titanates Na₂La₂Mn_xTi_{3-x}O₁₀ were synthesized via a standard ceramic technique using pre-calcined La₂O₃, MnO₂, TiO₂ and Na₂CO₃ as starting substances. The oxides were taken in stoichiometric amounts, and sodium carbonate was weighed with a variable excess to compensate for losses during calcination. All the reactants were mixed and ground in an agate mortar under an *n*-heptane layer at a rate 0.5 h per 1 g. The mixture obtained was dried and pelletized into ≈ 2 g tablets under the pressure of 50 bar using an Omec PI 88.00 hydraulic press (Certaldo, Italy). The tablets were placed into platinum crucibles with caps and calcined in a Nabertherm LHT 01/17 D (Lilienthal, Germany) muffle furnace. When the calcination included several stages, they were separated by intermediate grinding and re-pelletizing of the samples. After synthesis, the tablets were ground and rinsed with an excess of methanol, using sonication in a Elmasonic S10H bath (Elma, Singen, Germany) to purify the samples, removing the residual sodium carbonate. To obtain pure single-phase products, the optimization of the synthesis conditions (sodium excess, temperature, duration, number of calcination stages) was performed using several compositions as an example. All the variable parameters and their final values (marked “√”) that provided the highest phase purity of the products are summarized in Table 1.

Table 1. Tested conditions of Na₂La₂Mn_xTi_{3-x}O₁₀ synthesis.

Substitution Degree (x)	Excess of Na ₂ CO ₃ , %	T, °C	Number of Calcination Stages	Duration of Each Stage, h	Final Conditions
0	50	1100	2	12	√
		1050	2	12	

Table 1. Cont.

Substitution Degree (x)	Excess of Na_2CO_3 , %	T , °C	Number of Calcination Stages	Duration of Each Stage, h	Final Conditions
0.002–0.05	50	1100	3	12	✓
		1100	1	24	
		1050	2	12	
0.1–1.0	30	1100	2	12	
		1100	2	12	
	50	1050	1	24	
		1050	2	12	✓
		1000	2	12	

Using the final synthesis method optimized for the titanates with the substitution degrees $x = 0.1$ – 1.0 , we also studied the feasibility of obtaining similar substances with $x = 1.1$ – 1.7 .

2.2. Preparation of Protonated Titanates $(\text{H,Na})_2\text{La}_2\text{Mn}_x\text{Ti}_{3-x}\text{O}_{10}$ and Their Nanosheets

The methodology for protonation and exfoliation of the titanates into nanosheets was generally adopted from our previous publications [62,63].

To prepare protonated forms of the titanates, powders of $\text{Na}_2\text{La}_2\text{Mn}_x\text{Ti}_{3-x}\text{O}_{10}$ were placed in Petri dishes and spread in a thin layer. The samples were kept in a humid air atmosphere for 3 d and then washed several times with an excess of distilled water. After this, the samples were treated with 0.1 M HCl at a rate of 1 L of the solution per 5 g of the sample for 24 h. Afterwards, the protonated products $(\text{H,Na})_2\text{La}_2\text{Mn}_x\text{Ti}_{3-x}\text{O}_{10}$ were filtered under vacuum using hydrophilic Teflon filters and dried in air.

To obtain the exfoliated forms (nanosheets) of the titanates $(\text{H,Na})_2\text{La}_2\text{Mn}_x\text{Ti}_{3-x}\text{O}_{10}$, their methylamine derivatives were synthesized first. For this, 1 g of each sample was mixed with 20 mL of a 38% aqueous methylamine solution and treated in a laboratory microwave oven Milestone Ethos Easy (Soriso, Italy) at a temperature of 60 °C for 2 h. After cooling down and filtering, 160 mg of each methylamine derivative was mixed with 50 mL of 0.01 M aqueous tetrabutylammonium hydroxide TBAOH and subjected to sonication in a 200 W Hielscher UP200St homogenizer (Teltow, Germany) at a half power for 10 min. The mixtures obtained were kept under continuous stirring for 7 d, after which the sonication procedure was repeated. Then the suspensions of the target nanosheets were separated from bulk non-exfoliated fractions of the samples by centrifuging at a separation factor of 1000 RCF for 1 h in a laboratory centrifuge ELMI CM-6MT (Riga, Latvia) and removed with a pipette.

2.3. Investigation of Photophysical Characteristics

To find the bandgap energies E_g , diffuse reflectance spectra of the samples were transformed into coordinates $(F \cdot hv)^{1/2} = f(hv)$, where $F = (1 - R)^2/2R$ is the Kubelka–Munk function of a reflection coefficient R . Linear sections of low-energy regions of the Kubelka–Munk graphs were extrapolated to the intersection point whose abscissa was considered as the optical bandgap energy E_g [64].

The valence band maxima E_V vs. a standard hydrogen electrode (SHE) were approximately estimated using the formula $E_V = E_V' + W - 4.44$, where E_V' is the abscissa of the point obtained via the extrapolation of the linear sections of the valence band X-ray photoelectron spectrum at low binding energies, W is an instrumental work function and 4.44 eV is the relative shift of electron energy scales vs. a vacuum and SHE. The conduction band minima E_C vs. SHE were found according to the formula $E_C = E_V - E_g$ [65–67].

To evaluate the severity of radiative electron–hole recombination, average photoluminescence lifetimes τ were calculated based on the time-resolved photoluminescence spectra of the samples. For this, the luminescence decay graphs were fitted by a biexponential function $I(t) = A_1 \cdot \exp(-t/t_1) + A_2 \cdot \exp(-t/t_2) + I_0$. The τ values were found via the formula $\tau = (A_1 \cdot t_1^2 + A_2 \cdot t_2^2) / (A_1 \cdot t_1 + A_2 \cdot t_2)$, where A_n and t_n are the amplitudes and time constants, respectively, determined during fitting [68].

2.4. Investigation of Photocatalytic Activity with Respect to Hydrogen Production

The photocatalytic activity of the protonated titanates and their nanosheets was studied in the reaction of hydrogen production from 1 mol.% aqueous methanol under ultraviolet and visible irradiation using two light sources: a 125 W mercury lamp DRT-125 with a light filter transmitting $\lambda > 220$ nm, and a 100 W LED source with a wavelength of 425 nm. Detailed descriptions of the photocatalytic setting and emission spectra of the light sources used are presented in Information S1 and Figure S1, respectively. In all the photocatalytic experiments, Pt was used as a cocatalyst forming active sites of hydrogen evolution and improving the efficiency of spatial charge separation.

When testing the activity of the protonated titanates, 25 mg of each sample was dispersed in 49 mL of 1 mol.% aqueous methanol via sonication in a 60 W Elmasonic S10H bath (Elma, Singen, Germany) for 10 min. In the case of the exfoliated titanates, 47.8 mL of each suspension of their nanosheets (dispersed phase concentration ≈ 250 mg/L) was mixed with 1.2 mL of non-diluted methanol and adjusted to $\text{pH} \approx 7$ using a 1 M HCl solution. Further, the suspension obtained was pumped into the reaction cell, after which a magnetic stirrer, argon purging and the DRT-125 lamp were turned on. After 15 min, a fixed amount of a 1.28 mM H_2PtCl_6 solution was injected into the irradiated suspension to perform in situ photodeposition of Pt nanoparticles to the photocatalyst surface (1 mass. % in the resulting composite). A specific H_2PtCl_6 volume was chosen in accordance with the photocatalyst concentration in the reactor (1 mL for 500 mg/L protonated titanates, 0.5 mL for ≈ 250 mg/L exfoliated ones). Afterwards, the argon purging was continued for 30 min to remove all foreign gases. When testing the activity under visible light, the DRT-125 lamp was replaced with the LED source after finishing the platinization procedure. Then the argon purging was turned off and the photocatalytic measurement was started, consisting in online chromatographic hydrogen detection in the gaseous phase every 5 min. Some experiments additionally included a so-called dark stage, during which the light source was deliberately turned off to make sure that the photocatalytic reaction stops. In the end, the areas of hydrogen chromatographic peaks were converted to hydrogen amounts that, in turn, were used to plot kinetic curves. The latter were approximated by linear functions, whose slopes are equal to hydrogen evolution rates ω . Apparent quantum efficiencies of the reactions were calculated using the equation $\varphi = (2 \cdot \omega / f) \cdot 100\%$, where f is a lamp photon flux in the photocatalyst absorption range measured previously, as described in Information S2.

2.5. Instrumentation

2.5.1. XRD

Routine measurements of powder X-ray diffraction (XRD) patterns were performed using a Rigaku miniflex II benchtop Röntgen diffractometer (Tokyo, Japan) with Cu K α radiation, an angle range of $2\theta = 3\text{--}60^\circ$ and a scanning rate of $10^\circ/\text{min}$. For in-depth structural investigation, several samples were also analyzed by means of high-resolution X-ray diffractometry (HR-XRD) on Rigaku Ultima IV (Tokyo, Japan) using Cu K α radiation, an angle range of $2\theta = 3\text{--}120^\circ$ and a scanning rate of $2^\circ/\text{min}$. Phase composition of the samples was controlled using Rigaku PDXL 2.0 software and information resources of The International Centre for Diffraction Data (ICDD). Indexing of the diffraction patterns, calculation of the lattice parameters as well as Rietveld refinement of the crystal structure were carried out using DiffracPlus Topas 4.2 software (Bruker, Karlsruhe, Germany).

2.5.2. Raman Spectroscopy

Raman scattering spectra were recorded on a Bruker Senterra spectrometer (BillERICA, MA, USA) in the spectral range of $100\text{--}1000\text{ cm}^{-1}$ using a 785 nm solid-state laser (power 10 mW, single accumulation time 60 s, 4 repetitions).

2.5.3. ICP-AES

The elemental composition of the samples was controlled by inductively coupled plasma atomic emission spectroscopy (ICP-AES) on a Shimadzu ICPE-9000 spectrometer (Kyoto, Japan) after their microwave-assisted dissolution in 12 M HCl.

2.5.4. SEM-EDX

The morphology and elemental composition of the samples were additionally studied using a Zeiss Merlin scanning electron microscope (SEM) (Oberkochen, Germany) equipped with an Oxford Instruments INCAx-act energy-dispersive X-ray microanalyzer (EDX) (Abingdon, UK).

2.5.5. TG

Thermogravimetric (TG) analysis was performed on a Netzsch TG 209 F1 Libra thermobalance (Selb, Germany) in a synthetic air atmosphere. The temperature program included heating from room temperature to 950°C at a rate of $10^\circ\text{C}/\text{min}$ followed by a 20 min isotherm at 950°C to establish a constant mass.

2.5.6. DRS

Diffuse reflectance spectra (DRS) were recorded on a Perkin Elmer Lambda 1050 spectrophotometer (Waltham, MA, USA) equipped with a branded 150 mm InGaAs integrating sphere in the range of $200\text{--}2500\text{ nm}$ after sample deposition on a barium sulfate substrate.

2.5.7. XPS

X-ray photoelectron spectra (XPS), including those of the valence band region (VB-XPS), were measured on a Thermo Fisher Scientific Escalab 250Xi spectrometer (Waltham, MA, USA) with a monochromatized Al K α X-ray source ($h\nu = 1486.6\text{ eV}$) and binding energy scale calibration on a C 1s peak at 284.8 eV .

2.5.8. TR-PLS

Time-resolved photoluminescence spectroscopy (TR-PLS) was performed using a Horiba Jobin Yvon Fluorolog-3 spectrofluorometer (Kyoto, Japan). The samples were excited by a 340 nm pulse light-emitting diode, and the photoluminescence decays were measured at 415 nm.

3. Results and Discussion

3.1. Structure and Composition of the Mn-Containing Titanates

To achieve high phase purity of the target titanates, the conditions of their high-temperature ceramic synthesis were varied in accordance with Table 1. The final conditions providing preparation of the products not containing any detectable crystalline impurities were marked with a tick (✓). Generally, it was found that synthesis of the samples without manganese and with low substitution degrees ($x < 0.1$) requires a slightly higher temperature than that of the other compounds ($x \geq 0.1$). All the products obtained were identified by means of powder XRD analysis. Diffraction patterns of the initial and Mn-containing titanates are presented in Figure 1a ($0.1 \leq x \leq 1.0$) and Figure S2a ($0.002 \leq x \leq 0.05$). As one can see, all the patterns are generally similar to each other and are consistent with those in the literature for unmodified titanate (ICDD card № 01-082-2323). All the diffraction peaks observed were successfully indexed in the tetragonal system ($I4$ space group), and no significant impurities were detected. Table 2 summarizes the calculated unit cell parameters for the compounds with different manganese content x . The experimental data indicate that the partial substitution of titanium with manganese does not induce substantial structural transformations and the space group stays unchanged. However, there is a tendency for the parameter c to decrease with increasing manganese content, which can be attributed to the smaller Shannon's crystal radius of manganese (0.670 Å) compared to that of titanium (0.745 Å) in the corresponding coordination environment [69].

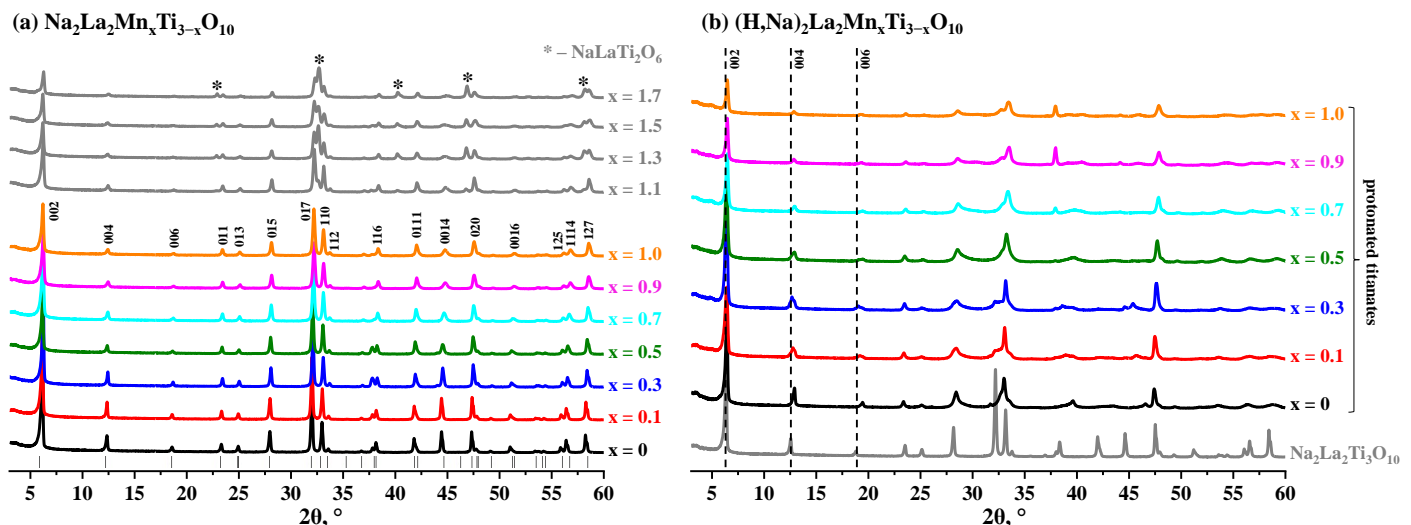


Figure 1. XRD patterns of alkaline (a) and protonated (b) forms of the titanates.

Attempts to synthesize the titanates with higher substitution degrees ($x > 1.0$) resulted in the appearance in the products of an impurity phase $\text{NaLaTi}_2\text{O}_6$ (Figure 1a). Thus, the manganese content $x = 1.0$ («by loading») proved to be the highest achievable for the titanates in question. This result is fully consistent with the previous literature reports on titanium substitution with manganese and ruthenium in the structurally related titanates, whose authors indicated the inevitable formation of undesirable by-phases when attempting to exceed the value $x = 1.0$ [60,61].

The alkaline titanates prepared were converted into so-called protonated forms, $(\text{H,Na})_2\text{La}_2\text{Mn}_x\text{Ti}_{3-x}\text{O}_{10}$, via the substitution of interlayer sodium cations with protons in a diluted hydrochloric acid. Comparative analysis of the XRD patterns of the alkaline and protonated compounds (Figure 1b and Figure S2b) revealed a shift of the $00l$ reflections towards higher diffraction angles. This shift indicates a decrease in the interlayer distance (in essence, the c parameter in Table 2) upon the protonation associated with the differ-

ence in the radii of sodium cations and protons. Although the patterns of the protonated titanates can be satisfactorily indexed in the tetragonal system with $a = b = 3.8 \text{ \AA}$, it was found that the peak positions observed are better described in the orthorhombic symmetry ($a \neq b$, Table 2).

Table 2. Lattice parameters of alkaline and protonated forms of the titanates.

x	$\text{Na}_2\text{La}_2\text{Mn}_x\text{Ti}_{3-x}\text{O}_{10}$ (Tetragonal)		$(\text{H,Na})_2\text{La}_2\text{Mn}_x\text{Ti}_{3-x}\text{O}_{10}$ (Orthorhombic)		
	$a = b, \text{ \AA}$	$c, \text{ \AA}$	$a, \text{ \AA}$	$b, \text{ \AA}$	$c, \text{ \AA}$
0	3.8	28.5	7.7	3.2	27.3
0.1	3.8	28.5	5.5	5.3	27.7
0.3	3.8	28.4	5.4	5.4	28.0
0.5	3.8	28.5	5.5	5.2	27.8
0.7	3.8	28.3	3.8	6.8	27.3
0.9	3.8	28.3	4.3	8.1	27.3
1.0	3.8	28.2	5.6	5.2	27.5

Further structural investigation of the alkaline titanates obtained was carried out using the Rietveld full-profile analysis. It was performed for the unmodified compound $\text{Na}_2\text{La}_2\text{Ti}_3\text{O}_{10}$ and selected Mn-substituted samples with relatively high manganese contents ($x = 0.5$ and $x = 0.9$). The previously reported structure of $\text{Na}_2\text{La}_2\text{Ti}_3\text{O}_{10}$ [70] served as a starting model. Firstly, the refinement of the undoped sample was performed using originally reported $I4/mmm$ and $I4$ space groups. While the literature reports a fit in a $I4/mmm$ group with a weighted profile R-factor (Rwp) of 12.87%, in our case, the best Rwp = 9.03% was achieved (Figure 2a). Peak shapes were mostly satisfactorily described by a pseudo-Voigt function using a Stephens model of anisotropic peak broadening. Since layered oxides tend to form plate-like particles with high texturing, which affects peak intensities in XRD patterns, a preferred orientation along 001 and 011 planes was applied to negate these effects in the final fitting.

The refined models based on $I4$ and $I4/mmm$ space groups then were applied to the Mn-containing titanates with $x = 0.5$ and $x = 0.9$ (Figure 2b,c) in order to additionally confirm the substitution of titanium by manganese, as well as determine its content and position in the structure. Refinement of the Ti/Mn occupancies showed that best fits were achieved for the models where Mn^{4+} cations substitute the Ti^{4+} ones in the middle sublayer of perovskite blocks and manganese content is close to the theoretical (0.4 for $x = 0.5$ and 0.8 for $x = 0.9$). As in case of the initial titanate $\text{Na}_2\text{La}_2\text{Ti}_3\text{O}_{10}$, the best Rwp factors for the Mn-containing materials were achieved using the $I4/mmm$ space group. The refined parameters are presented in the Table 3. As one can see, their values for $\text{Na}_2\text{La}_2\text{Ti}_3\text{O}_{10}$ are in good consistency with the literature ones. The substitution of Ti^{4+} by Mn^{4+} leads to a gradual decrease in the unit cell volume, which, as already noted above, is considered to be caused by the differences in size of six-coordinated octahedral Ti^{4+} (0.745 Å) and Mn^{4+} (0.670 Å) [69]. The structures refined are visualized in Figure 3, and the corresponding crystallographic information files (CIFs) are included in the Supplementary Materials (Information S3).

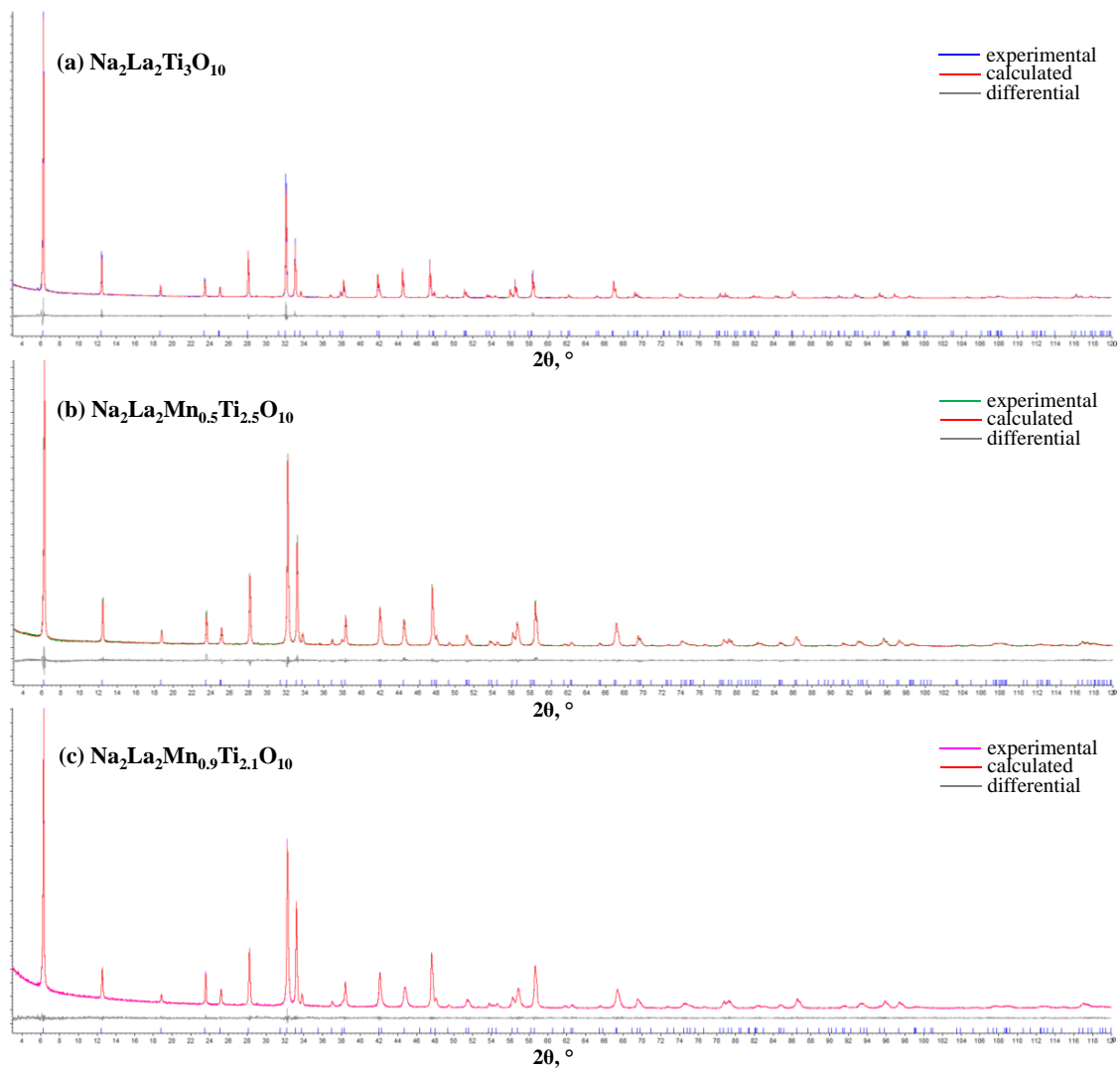


Figure 2. Rietveld refinement plots for the alkaline titanates with $x = 0$ (a), $x = 0.5$ (b) and $x = 0.9$ (c).

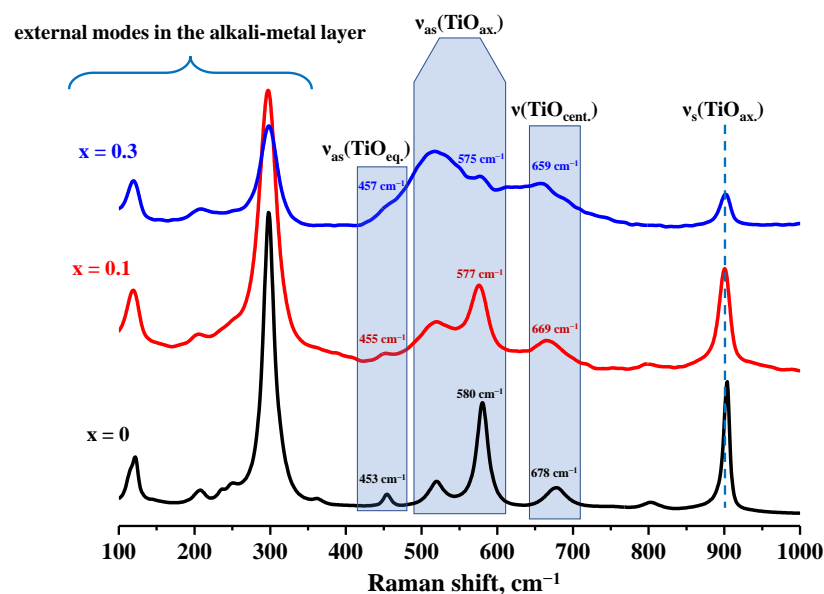


Figure 3. Refined structures of the alkaline titanates with $x = 0$ (a), $x = 0.5$ (b) and $x = 0.9$ (c).

Table 3. Parameters refined by the Rietveld method for the alkaline titanates with $x = 0, 0.5$ and 0.9 .

x	a , Å	c , Å	Unit Cell Volume, Å ³	Rwp, %
0 [70]	3.83528(7)	28.5737(7)	420.301	12.87
0	3.83882(0)	28.53078(2)	420.445	9.03
0.5	3.82617(2)	28.49389(9)	417.139	8.65
0.9	3.82276(7)	28.35898(7)	414.425	6.78

Raman spectra of the lattice vibrational modes ($100\text{--}1000\text{ cm}^{-1}$) of the alkaline titanates $\text{Na}_2\text{La}_2\text{Mn}_x\text{Ti}_{3-x}\text{O}_{10}$ ($x = 0, 0.1, 0.3$) are presented in Figure 4. The assignment of vibrational bands of the perovskite lattice was carried out based on data from the publication [71]. The bands below 400 cm^{-1} belong to the alkali metal vibrational modes in the interlayer space. The vibrations at 902 cm^{-1} are related to symmetric stretching of axial Ti–O bonds in terminal octahedra directed towards the interlayer space. These bands practically do not change their positions upon the titanium substitution with manganese in the perovskite sublattice. Meanwhile, the band of a slightly distorted central TiO_6 octahedra is seen to shift from 678 cm^{-1} to 669 cm^{-1} and 659 cm^{-1} when Mn is introduced into the structure in amounts of $x = 0.1$ and $x = 0.3$, respectively. The vibration band around 580 cm^{-1} is related to the stretching of axial Ti–O bonds in terminal octahedra directed towards the perovskite slab center. This band slightly shifts to 575 cm^{-1} with an increase in the manganese content. Finally, the band at 453 cm^{-1} is assigned to the asymmetric vibrations of equatorial Ti–O bonds in central TiO_6 octahedra. Upon the cationic substitution, this band insignificantly moves from 453 cm^{-1} to 455 cm^{-1} and 457 cm^{-1} . Raman spectra of the corresponding protonated titanates $(\text{H,Na})_2\text{La}_2\text{Mn}_x\text{Ti}_{3-x}\text{O}_{10}$ are shown in Figure S3. Although their bands are more broadened, they also reveal shifts of the perovskite sublattice modes accompanying the partial titanium substitution with manganese. The mentioned shifts of the lattice vibrational bands are consistent with the Rietveld refinement results and indicate that the manganese cations are embedded precisely into central octahedra of the perovskite block.

**Figure 4.** Raman spectra of the alkaline titanates with $x = 0, 0.1$ and 0.3 .

Quantitative compositions of both alkaline and protonated titanates were studied by means of ICP-AES (after acid digestion) and EDX (Table 4). The corresponding EDX spectra are presented in Figure S4. The analysis of the protonated samples was carried out to refute or confirm the potential existence of amorphous Mn-containing by-phases on the alkaline titanates' surface that are likely to dissolve during the protonation. Comparing the compositions of the alkaline and protonated compounds, one can see that the factual Mn:Ti ratios stay practically unchanged during the acid treatment, and the results obtained by the two different methods are in good agreement with each other. Since the manganese content in the alkaline and protonated titanates is quite close, it can be assumed that the main part of the detected manganese is indeed located in the perovskite lattice, not on the sample surface. Meanwhile, there is a slight discrepancy between the theoretical and experimental substitution degrees, indicating that manganese is still not completely incorporated into the structure and a small part of it might remain in the form of some amorphous impurities. The highest degree of substitution that was factually achieved was $x = 0.8$ – 0.9 , which corresponds to the degree «by loading» of 1.0.

Table 4. Factual Mn:Ti ratios in the alkaline and protonated titanates (normalized to La_2).

Theoretical Ratio Mn:Ti	$\text{Na}_2\text{La}_2\text{Mn}_x\text{Ti}_{3-x}\text{O}_{10}$		$(\text{H},\text{Na})_2\text{La}_2\text{Mn}_x\text{Ti}_{3-x}\text{O}_{10}$	
	ICP-AES	EDX	ICP-AES	EDX
0.0:3.0	0.00:3.05	0.0:3.1	0.00:3.04	0.0:3.1
0.1:2.9	0.09:2.91	0.1:3.0	0.08:2.87	0.1:3.0
0.3:2.7	0.26:2.77	0.3:2.9	0.26:2.71	0.3:2.8
0.5:2.5	0.44:2.52	0.5:2.6	0.43:2.51	0.4:2.6
0.7:2.3	0.61:2.31	0.6:2.4	0.59:2.29	0.6:2.4
0.9:2.1	0.78:2.10	0.8:2.1	0.75:2.08	0.8:2.1
1.0:2.0	0.86:2.01	0.9:2.0	0.84:1.99	0.8:2.0

The composition of the titanates $(\text{H},\text{Na})_2\text{La}_2\text{Mn}_x\text{Ti}_{3-x}\text{O}_{10}$ in terms of their protonation degree (completeness of sodium substitution with protons) and amount of intercalated water was additionally investigated by means of EDX and TG analysis (Table 5, Figure S5). The TG curves were processed using a technique reported in the literature [72] based on the assumption that the low-temperature stage of mass loss (approximately below 300 °C) mainly corresponds to the deintercalation of the interlayer water molecules, while the subsequent stage predominantly relates to the decomposition of the anhydrous compound. In accordance with this, the actual formulae of the protonated titanates under consideration should be presented as $\text{H}_{2x'}\text{Na}_{2-2x'}\text{La}_2\text{Mn}_x\text{Ti}_{3-x}\text{O}_{10}\cdot y\text{H}_2\text{O}$, where the protonation degree x' falls in the range of 0.70–0.95 and the intercalated water content y varies from 0.05 to 0.30 depending on the specific sample (Table 5). Moderate discrepancies in the protonation degrees found via the two methods could be associated with the semi-quantitative nature of EDX and potential changes in the manganese oxidation state during TG analysis. In general, the titanates with higher manganese contents were found to contain greater amounts of intercalated water.

XPS was employed to determine the oxidation state of manganese in the titanates. Figure 5a shows the core level Mn 2p spectra of the protonated samples $(\text{H},\text{Na})_2\text{La}_2\text{Mn}_x\text{Ti}_{3-x}\text{O}_{10}$ ($x = 0.3, 0.5, 0.7, 1.0$). The spectra contain two distinct peaks at 654.0 and 642.5 eV, corresponding to the spin-orbit doublets of Mn 2p_{1/2} and 2p_{3/2}, respectively. Deconvoluted Mn 2p_{3/2} peaks centered at 642.5 and 641.2 eV correspond to the Mn⁴⁺ and Mn³⁺ oxidation states, respectively [73]. A quantitative analysis of the

different oxidation state concentrations was conducted based on the integrated peak areas. The results indicate that the Mn^{4+} concentrations are 100%, 85%, 89%, 83%, and 93% for $x = 0.3, 0.5, 0.7, 0.9$ and 1.0 , respectively. The existence of some manganese ions in the Mn^{3+} state points to the presence of oxygen vacancies in the titanates obtained.

Table 5. Protonation degrees x' and amounts of intercalated water y in the protonated titanates.

Mn Content x	$\text{H}_{2x'}\text{Na}_{2-2x'}\text{La}_2\text{Mn}_x\text{Ti}_{3-x}\text{O}_{10}\cdot y\text{H}_2\text{O}$		
	x' (EDX)	x' (TG)	y (TG)
0	0.7	0.70	0.05
0.1	0.6	0.75	0.01
0.3	0.7	0.90	0.20
0.5	0.8	0.90	0.15
0.7	0.9	0.95	0.25
0.9	0.9	0.90	0.30
1.0	0.9	0.90	0.30

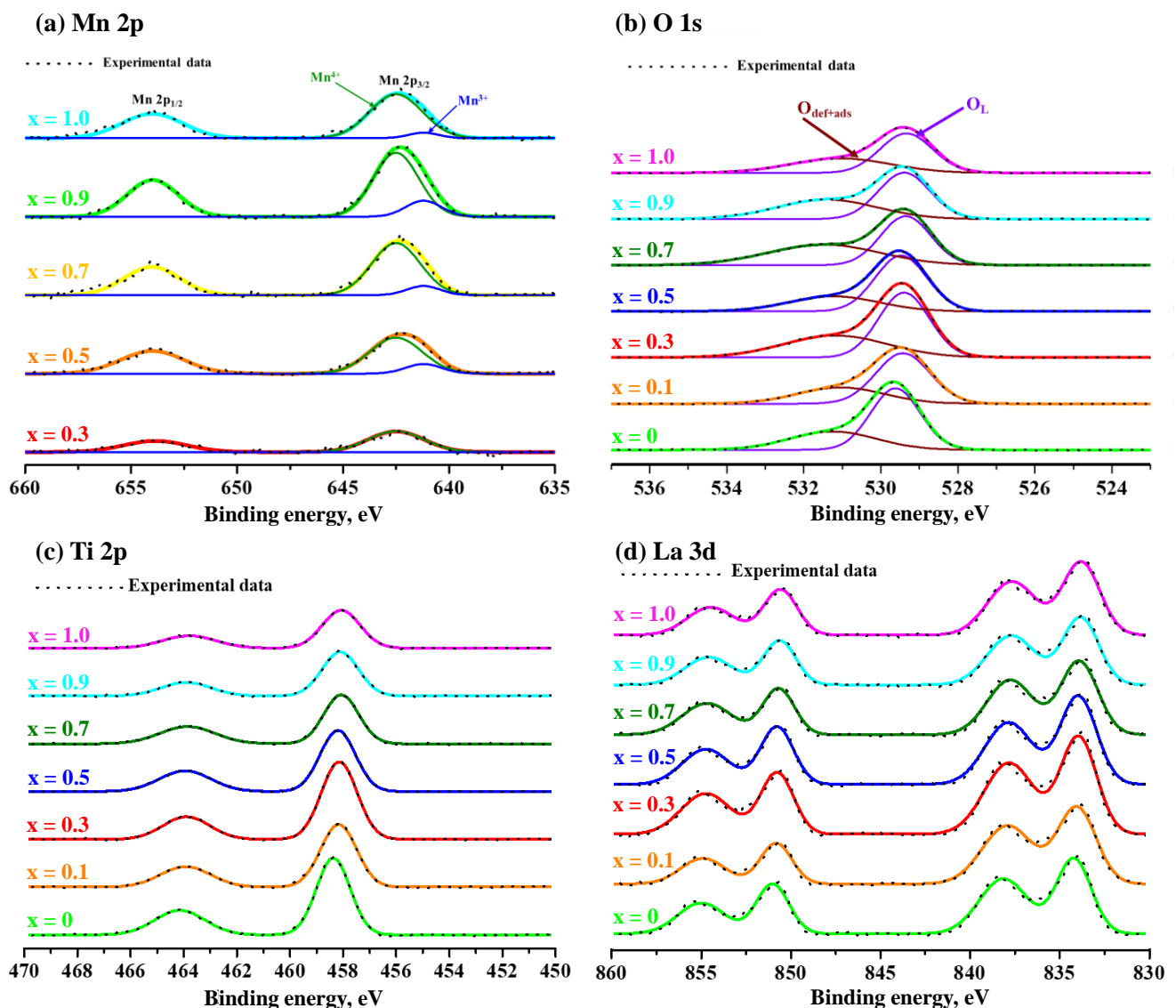


Figure 5. XPS of the protonated titanates: Mn 2p (a), O 1s (b), Ti 2p (c) and La 3d (d) regions.

Estimating the concentration of oxygen vacancies using XPS is a difficult task due to the similar binding energies of oxygen vacancies and adsorbed oxygen. Figure 5b presents the O 1s XPS of the protonated titanates. The deconvolution of the O 1s signal reveals the presence of the different contributions, including lattice oxygen (O_L) located at low binding energies (529.5 eV for $x = 0$), while the second contribution (531.2 eV for $x = 0$) includes oxygen vacancies, adsorbed oxygen, hydroxyl and carbonate groups on the surface ($O_{\text{def+ads}}$) [74]. The relative content of the lattice oxygen for each of the titanates is presented in Table 6. The results obtained do not demonstrate a clear correlation. However, the data indicate that the incorporation of manganese into the crystal structure for all the samples except $x = 0.1, 0.5$ led to a decrease in the proportion of the lattice oxygen, which could be associated with an increase in the number of defects.

Table 6. Relative content of lattice oxygen (O_L) in the protonated titanates.

x	Concentration of O_L , %
0.0	66
0.1	66
0.3	59
0.5	68
0.7	51
0.9	55
1.0	59

Figure 5c,d illustrate the La 3d and Ti 2p core-level XPS of the protonated titanates. The binding energy of La 3d (834.2 and 838.1 eV for La 3d_{5/2}, and 851.0 and 854.9 eV for La 3d_{3/2}) can be attributed to La^{3+} [75]. The Ti 2p spectrum shows Ti 2p_{3/2} and Ti 2p_{1/2} peaks at approximately 458.4 and 464.2 eV, respectively, which can be recognized as Ti^{4+} [76]. Incorporating manganese into the structure does not lead to a significant change in the appearance of the La 3d and Ti 2p spectra.

The morphology of the titanates obtained was studied using SEM (Figure S6). It is seen that particles of all the materials have a similar plate-like shape that is typical of layered oxides [77]. The samples represent polydisperse powders with lateral particle dimensions of 0.4–2 μm and a thickness of 200–600 nm. A comparison of the unmodified and Mn-containing titanates indicates that all the materials have a similar morphology, which does not change significantly during the protonation process.

3.2. Photophysical Properties of the Mn-Containing Titanates

Further photophysical characterization and photocatalytic investigation was performed for the protonated forms of the titanates that, unlike the alkaline precursors, are stable in aqueous media with respect to the interlayer ion exchange.

The range of intrinsic light absorption of the protonated titanates was studied by means of DRS with the Kubelka–Munk transformation of the spectra obtained (Figures 6a and S7a). As one can see from Table 7, the optical bandgap energy E_g of the initial unmodified sample ($x = 0$) is 3.20 eV, which allows it to function as a photocatalyst utilizing only mid-near ultraviolet with wavelengths up to 388 nm. Meanwhile, the partial substitution of Ti with Mn leads to a sharply pronounced band gap contraction. Particularly, even extremely low Mn contents ($x = 0.002$ – 0.005) prove to be already sufficient to shift the long-wave absorption edge of the samples to the visible range ($E_g < 3$ eV, $\lambda_{\text{max}} > 410$ nm). With a further increase in the substitution degree x , the absorption maximum rises monotonically and, starting from $x = 0.5$, the titanates acquire the ability to absorb even near-infrared

light. That being said, the absorption maximum achieved is 919 nm at $x = 1.0$. Thus, the insertion of Mn into the perovskite sublattice turned out to be an effective approach to expand the spectral area of potential operation of photocatalysts based on the titanates in question, which is of great importance for utilizing the visible and near-infrared parts of solar radiation.

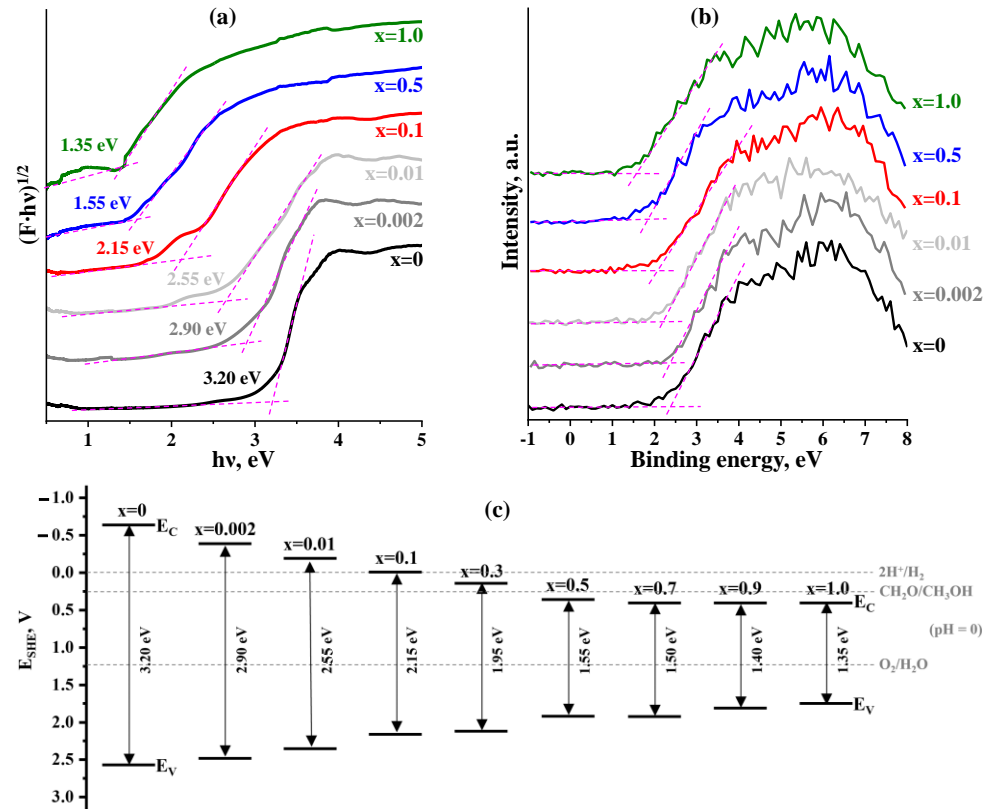


Figure 6. Kubelka–Munk plots (a), VB-XPS (b) and band edge diagrams (c) for the protonated titanates.

Table 7. Optical bandgap energies E_g , long-wave edges of intrinsic light absorption λ_{\max} , band edge potentials E_V and E_C vs. SHE, and average photoluminescence lifetimes τ at 340 nm excitation for the protonated titanates.

x	E_g , eV	λ_{\max} , nm	E_V , V	E_C , V	τ , μs
0	3.20	388	2.55	−0.65	3.32
0.002	2.90	428	2.50	−0.40	—
0.005	2.65	468	—	—	—
0.01	2.55	486	2.35	−0.20	—
0.025	2.45	506	—	—	—
0.05	2.30	539	—	—	—
0.1	2.15	577	2.15	0.00	3.37
0.3	1.95	636	2.10	0.15	—
0.5	1.55	800	1.90	0.35	3.47
0.7	1.50	827	1.90	0.40	—
0.9	1.40	886	1.80	0.40	—
1.0	1.35	919	1.75	0.40	3.69

The band edge potentials E_V and E_C of the protonated titanates were approximately estimated based on the above E_g values and VB-XPS data (Figures 6b and S7b). As can be seen from Figure 6c, the partial substitution of Ti with Mn is accompanied by shifts of both E_V and E_C values, which indicates participation of the Mn orbitals in the formation of both energy bands. Particularly, when moving from $x = 0$ to $x = 1.0$, the valence band top changes from 2.55 to 1.75 V and the conduction band bottom shifts from -0.65 to 0.40 V vs. SHE. Despite the incredibly wide light absorption range, the aforementioned displacement of the band edge potentials upon Mn insertion may adversely affect the possibility of using the corresponding photocatalysts in some practically valuable reactions. For instance, the E_C value of the titanates with $x \geq 0.3$ is more positive than the standard $2H^+/H_2$ reduction potential (0 V vs. SHE at pH = 0, 0.41 V vs. SHE at pH = 7), which may limit their use in hydrogen production reactions. At the same time, the samples with lower Mn contents ($x = 0.002$ – 0.01) should be, in principle, capable of functioning as hydrogen evolution photocatalysts at least in weakly acidic reaction media.

The intensity of the radiative electron–hole recombination in the protonated titanates was indirectly estimated using TR-PLS with excitation in the intrinsic absorption area (Figure 7). It was found that all the samples, being excited at $\lambda = 340$ nm, exhibit pronounced photoluminescence peaks at 400–450 nm, whose shape and position are practically independent of the Mn content in the compounds. Meanwhile, the partial substitution of Ti with Mn results in a slight increase in the average photoluminescence lifetime τ from 3.32 μ s at $x = 0$ to 3.69 μ s at $x = 1.0$ (Table 7). Thus, the insertion of Mn, apparently, does not increase the electron–hole recombination rate, although Mn is a foreign element in the crystal structure of the titanates that is potentially capable of being one of the recombination centers. This result is consistent with previous reports on cationic substitution (doping) in the structure of other perovskites, which was shown to improve charge carrier dynamics and separation efficiency [78,79].

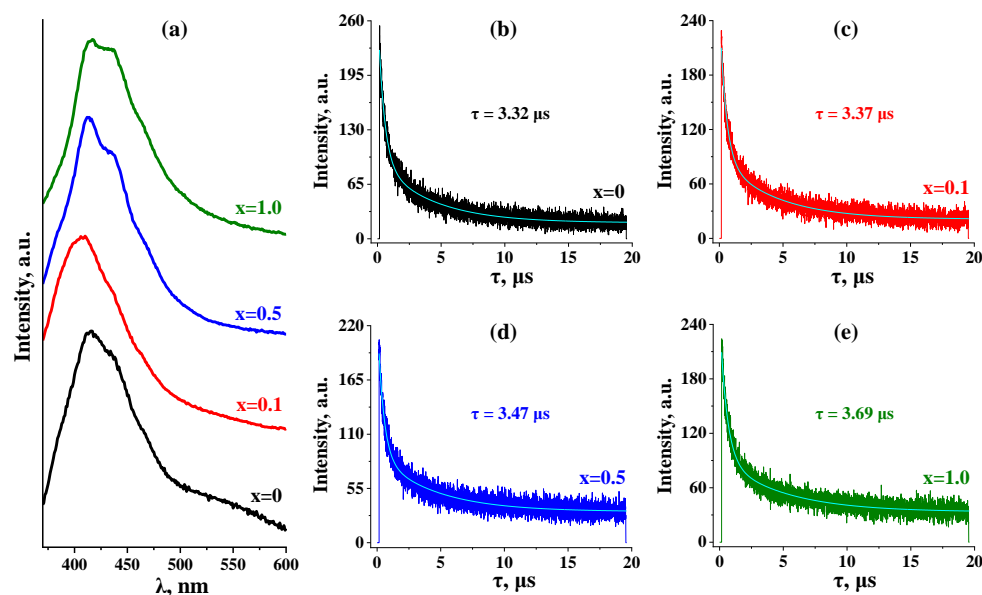


Figure 7. Photoluminescence spectra measured with 340 nm excitation (a), and decay graphs (b–e) for the protonated titanates with $x = 0, 0.1, 0.5$ and 1.0 .

3.3. Photocatalytic Activity of the Mn-Containing Titanates with Respect to Hydrogen Production

The photocatalytic properties of the protonated titanates and their exfoliated forms (nanosheets) were evaluated in the reactions of light-driven hydrogen evolution from 1% (mol.) aqueous methanol under the irradiation of a DRT-125 mercury lamp ($\lambda > 220$ nm) and

LED source ($\lambda = 425$ nm). All the materials were subjected to the in situ platinumization (1% Pt in the final composites) aimed at improving the spatial charge separation and creating active sites of hydrogen formation [80]. The resulting kinetics curves of photocatalytic hydrogen generation are presented in Figures 8 and S8. The rates and apparent quantum efficiencies of the reactions are summarized in Table 8 and visualized as bar graphs in Figure 9.

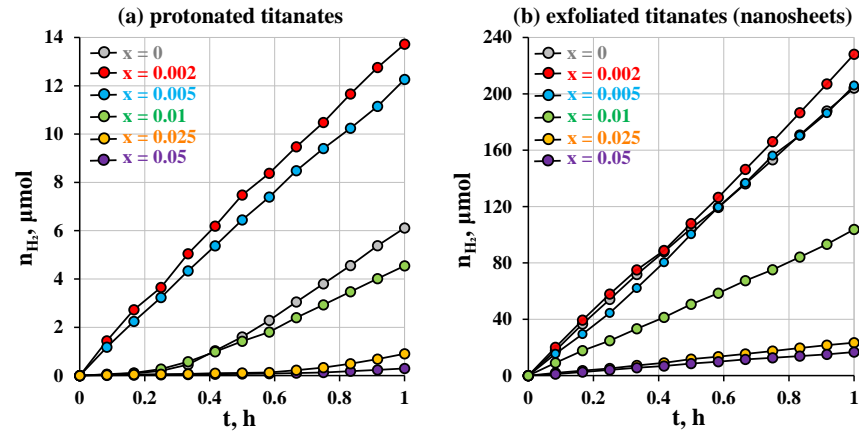


Figure 8. Kinetic curves of photocatalytic hydrogen evolution from 1% (mol.) aqueous methanol over platinumized protonated (a) and exfoliated (b) titanates with Mn content $0 \leq x \leq 0.05$ under DRT-125 lamp irradiation ($\lambda > 220$ nm).

Table 8. Photocatalytic activity of platinumized protonated and exfoliated titanates in 1% (mol.) aqueous methanol (hydrogen production rates ω and apparent quantum efficiencies φ) under the irradiation of a DRT-125 lamp ($\lambda > 220$ nm) and LED source ($\lambda = 425$ nm).

Mn (x)	DRT-125 ($\lambda > 220$ nm)						LED ($\lambda = 425$ nm)			
	Protonated Titanates			Exfoliated Titanates (Nanosheets)			Protonated Titanates		Exfoliated Titanates (Nanosheets)	
	ω		$\varphi, \%$	ω		$\varphi, \%$	ω		ω	
$\mu\text{mol}\cdot\text{h}^{-1}$	$\mu\text{mol}\cdot\text{h}^{-1}\cdot\text{g}^{-1}$	$\mu\text{mol}\cdot\text{h}^{-1}$		$\mu\text{mol}\cdot\text{h}^{-1}\cdot\text{g}^{-1}$	$\mu\text{mol}\cdot\text{h}^{-1}$		$\mu\text{mol}\cdot\text{h}^{-1}\cdot\text{g}^{-1}$	$\mu\text{mol}\cdot\text{h}^{-1}$	$\mu\text{mol}\cdot\text{h}^{-1}\cdot\text{g}^{-1}$	
0	9.76	390	0.10	202	16,160	2.08	0	0	0	0
0.002	13.4	536	0.14	224	17,920	2.31	≈ 0.9	≈ 36	≈ 0.9	≈ 72
0.005	12.0	480	0.12	212	16,960	2.18	≈ 0.7	≈ 28	≈ 0.7	≈ 56
0.01	6.55	262	0.067	102	8160	1.05	≈ 0.4	≈ 16	≈ 0.5	≈ 40
0.025	2.28	91.2	0.023	24.0	1920	0.25				
0.05	0.66	26	0.007	17.0	1360	0.18				
0.1	0.42	17		14.6	1170	0.044				
0.3	0.33	13		0.59	47	0.002				
0.5	0.54	22		0.08	6.4		0	0	0	0
0.7	0.27	11	<0.002	0.07	5.6					
0.9	0.64	26		0.11	8.8	<0.001				
1.0	0.30	12		0.16	12.8					

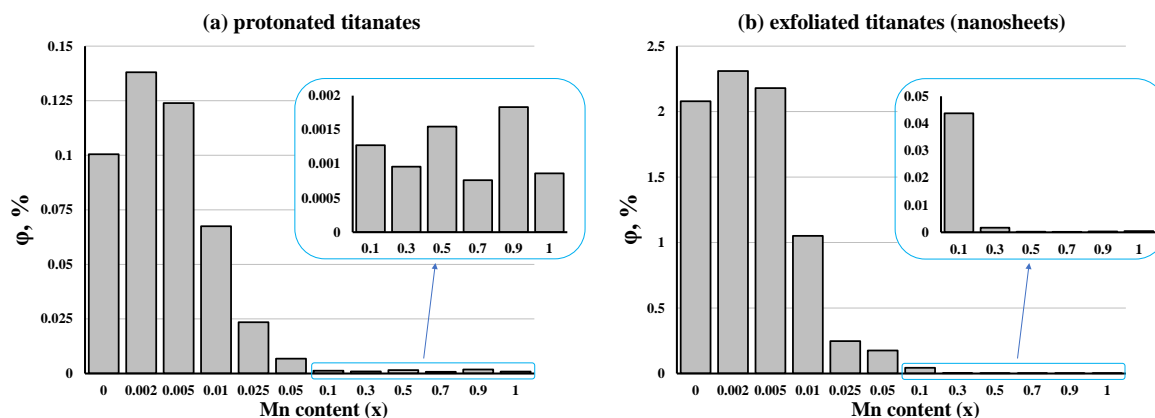


Figure 9. Apparent quantum efficiencies ϕ of photocatalytic hydrogen evolution from 1% (mol.) aqueous methanol over platinized protonated (a) and exfoliated (b) titanates under DRT-125 lamp irradiation ($\lambda > 220$ nm).

As can be seen from Figure 8, the hydrogen evolution curves over the most active photocatalysts demonstrate predominantly linear behavior throughout the whole measurement time. Meanwhile, some of the curves show a so-called activation period followed by the subsequent reaction rate growth, one of the reasons for which might be associated with a slow process of photocatalytic Pt reduction from H_2PtCl_6 . Some of the measurements also included dark stages (shown for the titanate with $x = 0$ in Figure S8) when the light source was turned off. After this, the kinetic curves gradually reach a plateau, indicating that the hydrogen generation stops.

It was established that the hydrogen evolution activity of the protonated titanates and their nanosheets under the DRT-125 lamp rises when moving from the unmodified sample ($x = 0$) to that with the lowest manganese content ($x = 0.002$) and then starts to decrease (Figure 9). That being said, the samples with $x = 0.002$ and $x = 0.005$ outperform the initial titanate in terms of both the hydrogen generation rate and apparent quantum efficiency. Moreover, the exfoliated forms of the titanates exhibit up to 20 times greater photocatalytic performance as compared to the protonated precursors with an equal Mn content (in the range $x \leq 0.05$), which is associated with the high specific surface area (small specific volume) of the nanosheets providing greater lifetimes of photogenerated electron-hole pairs and effective reactant adsorption. For instance, as shown in our previous publication [63], the exfoliated and reassembled titanate $\text{H}_2\text{La}_2\text{Ti}_3\text{O}_{10}$ possesses a more than 18-times higher specific surface area in comparison with that of the bulk precursor (60 vs. $3.2 \text{ m}^2/\text{g}$). Since the titanate nanosheets in this study are tested without preliminary reassembly, one can expect even greater differences in the active surface, explaining the pronounced improvement in the photocatalytic performance. However, the activity of the titanates and their nanosheets with $x > 0.1$ proved to be extremely low, despite the impressively wide range of intrinsic light absorption (Table 7). This result may be explained based on the energy diagrams of the corresponding semiconductor materials (Figure 6c): their conduction band minima E_C are located lower (are more positive) than the standard reduction potential $E^0(2\text{H}^+/\text{H}_2)$, which makes the hydrogen evolution reactions over these photocatalysts thermodynamically forbidden. In addition, the titanates with high Mn content may also contain amorphous impurities on the surface, adversely affecting the photocatalytic activity. These facts are also consistent with the photocatalytic activity of the titanates under purely visible irradiation of the LED source with $\lambda = 425$ nm. As can be seen from Table 8, the trace hydrogen amounts are evolved over the samples with low substitution degrees $0.002 \leq x \leq 0.01$, while the other materials do not provide the formation of any detectable hydrogen volumes.

Thus, low degrees of Ti substitution with Mn in the titanates (particularly, $x = 0.002$ and $x = 0.005$) turned out to be preferable for creating photocatalysts for hydrogen evolution. The corresponding materials, on the one hand, are capable of utilizing a wider range of irradiation than the unmodified compound and, on the other hand, their conduction band minimum still remains sufficiently negative to provide proton reduction. The aforementioned experimental fact is in good consistency with the numerous literature results indicating that the photocatalytic performance of cation-substituted layered perovskite-like oxides often passes through a maximum observed at relatively low substitution degrees. Particularly, this trend was confirmed by the Ti/Cr and Ti/Fe substitution in $\text{La}_2\text{Ti}_2\text{O}_7$ [81], Ti/Fe [59,82], Ti/Zn [56], Ti/V [57] and Ti/Nb [58] substitution in $\text{K}_2\text{La}_2\text{Ti}_3\text{O}_{10}$, and Nb/Mo substitution in $\text{HSr}_2\text{Nb}_3\text{O}_{10}$ [35], as well as Nb/Cr substitution in $\text{KSr}_2\text{Nb}_3\text{O}_{10}$ [36] and $\text{HPb}_2\text{Nb}_3\text{O}_{10}$ [83]. However, the Mn-substituted titanates with greater Mn content obtained may be of great interest for other photocatalytic reactions (for instance, water purification from organic pollutants) [84] or use in fuel cells [85]. Moreover, their representatives with high Mn contents are practically black, which makes them promising materials for thermo-assisted photocatalysis aiming to utilize the thermal energy of the sun to accelerate photocatalytic processes [86–89].

4. Conclusions

In the present study, a series of layered perovskite-like titanates, $\text{Na}_2\text{La}_2\text{Mn}_x\text{Ti}_{3-x}\text{O}_{10}$, as well as their protonated and exfoliated forms, has been prepared with various degrees substitution of titanium with manganese ($x = 0.002$ – 1.0). It was established that the Mn^{4+} cations are embedded in the middle sublayer of oxygen octahedra in the perovskite slabs, $\text{La}_2\text{Mn}_x\text{Ti}_{3-x}\text{O}_{10}^{2-}$, and the actual achievable manganese content x in the products is ≈ 0.9 . The partial cationic substitution in the perovskite sublattice leads to a pronounced contraction of the optical band gap from 3.20 to 1.35 eV (depending on x) and, therefore, allows the corresponding compounds to absorb not only ultraviolet, but also visible and near-infrared light with wavelengths up to ≈ 920 nm. The materials obtained have been tested as photocatalysts of hydrogen evolution from aqueous methanol, and the greatest activity in this reaction was demonstrated by the samples with low manganese contents $x = 0.002$ – 0.01 . The corresponding materials are, on the one hand, capable of utilizing a wider range of irradiation than the unmodified compound, while on the other hand, their conduction band minimum still remains sufficiently negative to provide proton reduction. However, the titanates with greater substitution degrees may be of high interest for use in other photocatalytic processes and, especially, in thermophotocatalysis due to the improved ability to absorb the near-infrared part of solar radiation.

Supplementary Materials: The following supporting information can be downloaded at <https://www.mdpi.com/article/10.3390/solids6020023/s1>. Figure S1: Emission spectra of the light sources used in photocatalytic experiments; Figure S2: XRD patterns of the alkaline and protonated titanates with low Mn content ($x < 0.1$); Figure S3: Raman spectra of the protonated titanates with $x = 0, 0.1$ and 0.3 ; Figure S4: EDX spectra of the alkaline and protonated titanates; Figure S5: TG curves of the protonated titanates; Figure S6: SEM images of the alkaline and protonated titanates; Figure S7: Kubelka–Munk plots and VB-XPS for the protonated titanates; Figure S8: Kinetic curves of photocatalytic hydrogen evolution from 1% (mol.) aqueous methanol over the protonated and exfoliated titanates; Information S1: Scheme and operating principle of the photocatalytic setting; Information S2: Determination of the lamp photon flux; Information S3: Crystallographic information files (CIFs) for the alkaline titanates refined by the Rietveld method.

Author Contributions: Conceptualization, O.I.S. and I.A.M.; methodology, S.A.K., V.V.V. and A.I.U.; validation, S.A.K. and O.I.S.; investigation, V.V.V., A.I.U., S.A.K., I.A.M., D.V.P., O.V.V. and A.V.K.; resources, O.I.S. and I.A.Z.; data curation, S.A.K. and O.I.S.; writing—original draft preparation, S.A.K., V.V.V., A.I.U., I.A.M. and O.I.S.; writing—review and editing, S.A.K. and O.I.S.; visualization, S.A.K., V.V.V., A.I.U. and I.A.M.; supervision, S.A.K., O.I.S. and I.A.Z.; project administration, O.I.S. and I.A.Z.; funding acquisition, O.I.S. All authors have read and agreed to the published version of the manuscript.

Funding: This research and the APC were funded by the Russian Science Foundation, grant number 22-73-10110.

Data Availability Statement: The research data are available in the article body and Supplementary Materials.

Acknowledgments: This research was conducted using the equipment of the Saint Petersburg State University Research Park: Center for X-ray Diffraction Studies, Center for Optical and Laser Materials Research, Center for Chemical Analysis and Materials Research, Center for Thermal Analysis and Calorimetry, Interdisciplinary Center for Nanotechnology, Center for Studies in Surface Science, and Center for Diagnostics of Functional Materials for Medicine, Pharmacology and Nanoelectronics.

Conflicts of Interest: The authors declare no conflicts of interest.

References

1. Irshad, M.; Ain, Q.T.; Zaman, M.; Aslam, M.Z.; Kousar, N.; Asim, M.; Rafique, M.; Siraj, K.; Tabish, A.N.; Usman, M.; et al. Photocatalysis and Perovskite Oxide-Based Materials: A Remedy for a Clean and Sustainable Future. *RSC Adv.* **2022**, *12*, 7009–7039. [[CrossRef](#)]
2. Schaak, R.E.; Mallouk, T.E. Perovskites by Design: A Toolbox of Solid-State Reactions. *Chem. Mater.* **2002**, *14*, 1455–1471. [[CrossRef](#)]
3. Uppuluri, R.; Sen Gupta, A.; Rosas, A.S.; Mallouk, T.E. Soft Chemistry of Ion-Exchangeable Layered Metal Oxides. *Chem. Soc. Rev.* **2018**, *47*, 2401–2430. [[CrossRef](#)]
4. Campbell, K.D. Layered and Double Perovskites as Methane Coupling Catalysts. *Catal. Today* **1992**, *13*, 245–253. [[CrossRef](#)]
5. Rodionov, I.A.; Zvereva, I.A. Photocatalytic Activity of Layered Perovskite-like Oxides in Practically Valuable Chemical Reactions. *Russ. Chem. Rev.* **2016**, *85*, 248–279. [[CrossRef](#)]
6. Hinterding, R.; Feldhoff, A. Two-Dimensional Oxides: Recent Progress in Nanosheets. *Z. Für Phys. Chem.* **2018**, *233*, 117–165. [[CrossRef](#)]
7. Hu, Y.; Mao, L.; Guan, X.; Tucker, K.A.; Xie, H.; Wu, X.; Shi, J. Layered Perovskite Oxides and Their Derivative Nanosheets Adopting Different Modification Strategies towards Better Photocatalytic Performance of Water Splitting. *Renew. Sustain. Energy Rev.* **2020**, *119*, 109527. [[CrossRef](#)]
8. Singh, S.J.; Jayaram, R.V. Chemoselective O-Tert-Butoxycarbonylation of Hydroxy Compounds Using NaLaTiO₄ as a Heterogeneous and Reusable Catalyst. *Tetrahedron Lett.* **2008**, *49*, 4249–4251. [[CrossRef](#)]
9. Tasleem, S.; Tahir, M. Current Trends in Strategies to Improve Photocatalytic Performance of Perovskites Materials for Solar to Hydrogen Production. *Renew. Sustain. Energy Rev.* **2020**, *132*, 110073. [[CrossRef](#)]
10. Krashennikova, O.V.; Syrov, E.V.; Smirnov, S.M.; Suleimanov, E.V.; Fukina, D.G.; Knyazev, A.V.; Titaev, D.N. Synthesis, Crystal Structure and Photocatalytic Activity of New Dion-Jacobson Type Titanoniobates. *J. Solid State Chem.* **2022**, *315*, 123445. [[CrossRef](#)]
11. Thangadurai, V.; Shukla, A.; Gopalakrishnan, J. Proton Conduction in Layered Perovskite Oxides. *Solid State Ion.* **1994**, *73*, 9–14. [[CrossRef](#)]
12. Toda, K.; Watanabe, J.; Satoh, M. Synthesis and Ionic Conductivity of New Layered Perovskite Compound, Ag₂La₂Ti₃O₁₀. *Solid State Ion.* **1996**, *90*, 15–19. [[CrossRef](#)]
13. Sato, M.; Abo, J.; Jin, T.; Ohta, M. Structure and Ionic Conductivity of mLaNb₂O₇ (M-K, Na, Li, H). *J. Alloys Compd.* **1993**, *192*, 81–83. [[CrossRef](#)]
14. Toda, K.; Suzuki, T.; Sato, M. Synthesis and High Ionic Conductivity of New Layered Perovskite Compounds, AgLaTa₂O₇ and AgCa₂Ta₃O₁₀. *Solid State Ion.* **1997**, *93*, 177–181. [[CrossRef](#)]
15. Sato, M.; Watanabe, J.; Kazuyoshi, U. Crystal Structure and Ionic Conductivity of a Layered-Perovskite AgLaNb₂O₇. *J. Solid State Chem.* **1993**, *107*, 460–470. [[CrossRef](#)]
16. Peláiz-Barranco, A.; González-Abreu, Y. Ferroelectric Ceramic Materials of the Aurivillius Family. *J. Adv. Dielectr.* **2013**, *3*, 1330003. [[CrossRef](#)]

17. Moure, A. Review and Perspectives of Aurivillius Structures as a Lead-Free Piezoelectric System. *Appl. Sci.* **2018**, *8*, 62. [[CrossRef](#)]
18. Ida, S.; Ogata, C.; Eguchi, M.; Youngblood, W.J.; Mallouk, T.E.; Matsumoto, Y. Photoluminescence of Perovskite Nanosheets Prepared by Exfoliation of Layered Oxides, $K_2Ln_2Ti_3O_{10}$, $KLnNb_2O_7$, and $RbLnTa_2O_7$ (Ln: Lanthanide Ion). *J. Am. Chem. Soc.* **2008**, *130*, 7052–7059. [[CrossRef](#)]
19. Szczepanski, F.; Bayart, A.; Katelnikovas, A.; Blach, J.F.; Rousseau, J.; Saitzek, S. Luminescence and Up-Conversion Properties in $La_2Ti_2O_7:Eu^{3+},Er^{3+}$ Oxides under UV and NIR Radiations towards a Two-Color Sensor. *J. Alloys Compd.* **2020**, *826*, 154157. [[CrossRef](#)]
20. Yuan, M.; Dong, W.; Wei, L.; Liu, Q.; Meng, Y.; Wang, X.; Wang, B.; Zhu, B. Stability Study of SOFC Using Layered Perovskite Oxide $La_{1.85}Sr_{0.15}CuO_4$ Mixed with Ionic Conductor as Membrane. *Electrochim. Acta* **2020**, *332*, 135487. [[CrossRef](#)]
21. Bi, D.; Tress, W.; Dar, M.I.; Gao, P.; Luo, J.; Renevier, C.; Schenk, K.; Abate, A.; Giordano, F.; Baena, J.C.; et al. Efficient Luminescent Solar Cells Based on Tailored Mixed-Cation Perovskites. *Sci. Adv.* **2016**, *2*, e1501170. [[CrossRef](#)] [[PubMed](#)]
22. Constantino, V.R.L.; Barbosa, C.A.S.; Bizeto, M.A.; Dias, P.M. Intercalation Compounds Involving Inorganic Layered Structures. *An. Acad. Bras. Cienc.* **2000**, *72*, 45–49. [[CrossRef](#)] [[PubMed](#)]
23. Boykin, J.R.; Smith, L.J. Rapid Microwave-Assisted Grafting of Layered Perovskites with n-Alcohols. *Inorg. Chem.* **2015**, *54*, 4177–4179. [[CrossRef](#)] [[PubMed](#)]
24. Wang, Y.; Zhu, X.; Li, X.; Wang, L.; Wang, Y.; Hao, Q.; Tang, K. D-Glucopyranose-Modified Compound of Ruddlesden-Popper Phases $H_2CaTa_2O_7$: Characterization and Intercalation with Ag. *J. Mater. Chem. A* **2014**, *2*, 15590–15597. [[CrossRef](#)]
25. Takeda, Y.; Suzuki, H.; Notsu, K.; Sugimoto, W.; Sugahara, Y. Preparation of a Novel Organic Derivative of the Layered Perovskite Bearing $HLaNb_2O_7 \cdot nH_2O$ Interlayer Surface Trifluoroacetate Groups. *Mater. Res. Bull.* **2006**, *41*, 834–841. [[CrossRef](#)]
26. Jacobson, A.J.; Johnson, J.W.; Lewandowski, J. Intercalation of the Layered Solid Acid $HCa_2Nb_3O_{10}$ by Organic Amines. *Mater. Res. Bull.* **1987**, *22*, 45–51. [[CrossRef](#)]
27. Suzuki, H.; Notsu, K.; Takeda, Y.; Sugimoto, W.; Sugahara, Y. Reactions of Alkoxyl Derivatives of a Layered Perovskite with Alcohols: Substitution Reactions on the Interlayer Surface of a Layered Perovskite. *Chem. Mater.* **2003**, *15*, 636–641. [[CrossRef](#)]
28. Akbarian-Tefaghi, S.; Teixeira Veiga, E.; Amand, G.; Wiley, J.B.J.B. Rapid Topochemical Modification of Layered Perovskites via Microwave Reactions. *Inorg. Chem.* **2016**, *55*, 1604–1612. [[CrossRef](#)]
29. Tahara, S.; Ichikawa, T.; Kajiwarra, G.; Sugahara, Y. Reactivity of the Ruddlesden–Popper Phase $H_2La_2Ti_3O_{10}$ with Organic Compounds: Intercalation and Grafting Reactions. *Chem. Mater.* **2007**, *19*, 2352–2358. [[CrossRef](#)]
30. Matsuda, T.; Udagawa, M.; Kunou, I. Modification of the Interlayer in Lanthanum-Niobium Oxide and Its Catalytic Reactions. *J. Catal.* **1997**, *168*, 26–34. [[CrossRef](#)]
31. Kurnosenko, S.A.; Voytovich, V.V.; Silyukov, O.I.; Rodionov, I.A.; Kirichenko, S.O.; minich, I.A.; Malygina, E.N.; Khramova, A.D.; Zvereva, I.A. Photocatalytic Activity of N-Alkylamine and n-Alkoxy Derivatives of Layered Perovskite-like Titanates $H_2Ln_2Ti_3O_{10}$ (Ln = La, Nd) in the Reaction of Hydrogen Production from an Aqueous Solution of Methanol. *Catalysts* **2021**, *11*, 1279. [[CrossRef](#)]
32. Kurnosenko, S.A.; Voytovich, V.V.; Silyukov, O.I.; Rodionov, I.A.; Zvereva, I.A. Photocatalytic Hydrogen Production from Aqueous Solutions of Glucose and Xylose over Layered Perovskite-like Oxides $HCa_2Nb_3O_{10}$, $H_2La_2Ti_3O_{10}$ and Their Inorganic-Organic Derivatives. *Nanomaterials* **2022**, *12*, 2717. [[CrossRef](#)] [[PubMed](#)]
33. Machida, M.; Mitsuyama, T.; Ikeue, K.; Matsushima, S.; Arai, M. Photocatalytic Property and Electronic Structure of Triple-Layered Perovskite Tantalates, $MCa_2Ta_3O_{10}$ (M = Cs, Na, H, and $C_6H_{13}NH_3$). *J. Phys. Chem. B* **2005**, *109*, 7801–7806. [[CrossRef](#)] [[PubMed](#)]
34. Domen, K.; Ebina, Y.; Ikeda, S.; Tanaka, A.; Kondo, J.; Maruya, K. Layered Niobium Oxides Pillaring and Exfoliation. *Catal. Today* **1996**, *28*, 167–174. [[CrossRef](#)]
35. Xu, J.; Wei, Y.; Huang, Y.; Wang, J.; Chen, A.; Fan, L.; Wu, J. Microwave-Assisted Synthesis of Mo-Doped $H_{1-x}Sr_2Nb_{3-x}Mo_xO_{10}$ ($x = 0, 0.05, 0.1, 0.15$ and 0.2) with High Photocatalytic Activity. *J. Semicond.* **2014**, *35*, 083001. [[CrossRef](#)]
36. Hu, Y.; Guo, P.; Guo, L. Synthesis and Photocatalytic Properties of Cr-Doped $KSr_2Nb_3O_{10}$ for Hydrogen Production. *Int. J. Hydrogen Energy* **2012**, *37*, 1007–1013. [[CrossRef](#)]
37. Khlyustova, A.; Sirotkin, N.; Kusova, T.; Kraev, A.; Titov, V.; Agafonov, A. Doped TiO_2 : The Effect of Doping Elements on Photocatalytic Activity. *Mater. Adv.* **2020**, *1*, 1193–1201. [[CrossRef](#)]
38. Kumar, V.; Govind; Uma, S. Investigation of Cation (Sn^{2+}) and Anion (N^{3-}) Substitution in Favor of Visible Light Photocatalytic Activity in the Layered Perovskite $K_2La_2Ti_3O_{10}$. *J. Hazard. Mater.* **2011**, *189*, 502–508. [[CrossRef](#)]
39. Suzuki, H.; Tomita, O.; Higashi, M.; Nakada, A.; Abe, R. Improved Visible-Light Activity of Nitrogen-Doped Layered Niobate Photocatalysts by NH_3 -Nitridation with KCl Flux. *Appl. Catal. B Environ.* **2018**, *232*, 49–54. [[CrossRef](#)]
40. Suzuki, H.; Tomita, O.; Higashi, M.; Abe, R. Design of Nitrogen-Doped Layered Tantalates for Non-Sacrificial and Selective Hydrogen Evolution from Water under Visible Light. *J. Mater. Chem. A* **2016**, *4*, 14444–14452. [[CrossRef](#)]
41. Khan, M.S.; Diao, Z.; Osada, M.; Shen, S. Nitrogen Doped Ultrathin Calcium/Sodium Niobate Perovskite Nanosheets for Photocatalytic Water Oxidation. *Sol. Energy Mater. Sol. Cells* **2020**, *205*, 110283. [[CrossRef](#)]

42. Zong, X.; Sun, C.; Chen, Z.; Mukherji, A.; Wu, H.; Zou, J.; Smith, S.C.; Lu, G.Q.; Wang, L. Nitrogen Doping in Ion-Exchangeable Layered Tantalate towards Visible-Light Induced Water Oxidation. *Chem. Commun.* **2011**, *47*, 6293–6295. [[CrossRef](#)] [[PubMed](#)]
43. Huang, Y.; Wei, Y.; Cheng, S.; Fan, L.; Li, Y.; Lin, J.; Wu, J. Photocatalytic Property of Nitrogen-Doped Layered Perovskite $K_2La_2Ti_3O_{10}$. *Sol. Energy Mater. Sol. Cells* **2010**, *94*, 761–766. [[CrossRef](#)]
44. Zhou, Y.; Wen, T.; Guo, Y.; Yang, B.; Wang, Y. Controllable Doping of Nitrogen and Tetravalent Niobium Affords Yellow and Black Calcium Niobate Nanosheets for Enhanced Photocatalytic Hydrogen Evolution. *RSC Adv.* **2016**, *6*, 64930–64936. [[CrossRef](#)]
45. Ida, S.; Okamoto, Y.; Koga, S.; Hagiwara, H.; Ishihara, T. Black-Colored Nitrogen-Doped Calcium Niobium Oxide Nanosheets and Their Photocatalytic Properties under Visible Light Irradiation. *RSC Adv.* **2013**, *3*, 11521–11524. [[CrossRef](#)]
46. Pan, S.; Shi, J.; Zhang, M.; Wu, M.; Cen, Y.; Guo, W.; Zhu, Y. Photocatalytic Performance Enhancement of Two-Dimensional Ruddlesden-Popper Type Perovskite $K_2La_2Ti_3O_{10}$ by Nitrogen-Doping. *Mater. Res. Express* **2019**, *6*, 075047. [[CrossRef](#)]
47. Gopalakrishnan, J.; Bhat, V. $A_2Ln_2Ti_3O_{10}$ (A = Potassium or Rubidium; Ln = Lanthanum or Rare Earth): A New Series of Layered Perovskites Exhibiting Ion Exchange. *Inorg. Chem.* **1987**, *26*, 4299–4301. [[CrossRef](#)]
48. Takata, T.; Shinohara, K.; Tanaka, A.; Hara, M.; Kondo, J.N.; Domen, K. A Highly Active Photocatalyst for Overall Water Splitting with a Hydrated Layered Perovskite Structure. *J. Photochem. Photobiol. A Chem.* **1997**, *106*, 45–49. [[CrossRef](#)]
49. Cui, W.; Liu, L.; Ma, S.; Liang, Y.; Zhang, Z. CdS-Sensitized $K_2La_2Ti_3O_{10}$ Composite: A New Photocatalyst for Hydrogen Evolution under Visible Light Irradiation. *Catal. Today* **2013**, *207*, 44–49. [[CrossRef](#)]
50. Huang, Y.; Wu, J.; Wei, Y.; Lin, J.; Huang, M. Hydrothermal Synthesis of $K_2La_2Ti_3O_{10}$ and Photocatalytic Splitting of Water. *J. Alloys Compd.* **2008**, *456*, 364–367. [[CrossRef](#)]
51. Cui, W.; Qi, Y.; Liu, L.; Rana, D.; Hu, J.; Liang, Y. Synthesis of $PbS-K_2La_2Ti_3O_{10}$ Composite and Its Photocatalytic Activity for Hydrogen Production. *Prog. Nat. Sci. Mater. Int.* **2012**, *22*, 120–125. [[CrossRef](#)]
52. Yang, Y.H.; Qiu, G.Z.; Chen, Q.Y.; Feng, Q.M.; Yin, Z.L. Influence of Calcination Atmosphere on Photocatalytic Reactivity of $K_2La_2Ti_3O_{10}$ for Water Splitting. *Trans. Nonferrous Met. Soc. China* **2007**, *17*, 836–840. [[CrossRef](#)]
53. Cui, W.; Liu, L.; Feng, L.; Xu, C.; Li, Z.; Lü, S.; Qiu, F. Preparation of $Pt/K_2La_2Ti_3O_{10}$ and Its Photo-Catalytic Activity for Hydrogen Evolution from Methanol Water Solution. *Sci. China Ser. B* **2006**, *49*, 162–168. [[CrossRef](#)]
54. Tai, Y.-W.; Chen, J.-S.; Yang, C.-C.; Wan, B.-Z. Preparation of Nano-Gold on $K_2La_2Ti_3O_{10}$ for Producing Hydrogen from Photo-Catalytic Water Splitting. *Catal. Today* **2004**, *97*, 95–101. [[CrossRef](#)]
55. Thaminimulla, C. Effect of Chromium Addition for Photocatalytic Overall Water Splitting on $Ni-K_2La_2Ti_3O_{10}$. *J. Catal.* **2000**, *196*, 362–365. [[CrossRef](#)]
56. Ya-Hui, Y.; Qi-Yuan, C.; Zhou-Lan, Y.; Jie, L. Study on the Photocatalytic Activity of $K_2La_2Ti_3O_{10}$ Doped with Zinc(Zn). *Appl. Surf. Sci.* **2009**, *255*, 8419–8424. [[CrossRef](#)]
57. Yang, Y.; Chen, Q.; Yin, Z.; Li, J. Study on the Photocatalytic Activity of $K_2La_2Ti_3O_{10}$ Doped with Vanadium (V). *J. Alloys Compd.* **2009**, *488*, 364–369. [[CrossRef](#)]
58. Huang, Y.; Wu, J.; Wei, Y.; Hao, S.; Huang, M.; Lin, J. Synthesis and Photocatalytic Activity of Hydrated Layered Perovskite $K_{2-x}La_2Ti_{3-x}Nb_xO_{10}$ ($x = 0-1$) and Protonated Derivatives. *Scr. Mater.* **2007**, *57*, 437–440. [[CrossRef](#)]
59. Wang, B.; Li, C.; Hirabayashi, D.; Suzuki, K. Hydrogen Evolution by Photocatalytic Decomposition of Water under Ultraviolet-Visible Irradiation over $K_2La_2Ti_{3-x}M_xO_{10+\delta}$ Perovskite. *Int. J. Hydrogen Energy* **2010**, *35*, 3306–3312. [[CrossRef](#)]
60. Lalena, J.N.; Falster, A.U.; Simmons, W.B., Jr.; Carpenter, E.E.; Wiggins, J.; Hariharan, S.; Wiley, J.B. Synthesis and Characterization of New Mixed-Metal Triple-Layered Perovskites, $Na_2La_2Ti_{3-x}Ru_xO_{10}$ ($x \leq 1.0$). *Chem. Mater.* **2000**, *27*, 2418–2423. [[CrossRef](#)]
61. Schaak, R.E.; Afzal, D.; Schottenfeld, J.A.; Mallouk, T.E. $Na_2Ln_2Ti_{3-x}Mn_xO_{10}$ (Ln = Sm, Eu, Gd, and Dy; $0 \leq x \leq 1$): A New Series of Ion-Exchangeable Layered Perovskites Containing B-Site Manganese. *Chem. Mater.* **2002**, *14*, 442–448. [[CrossRef](#)]
62. Kurnosenko, S.A.; minich, I.A.; Silyukov, O.I.; Zvereva, I.A. Highly Efficient Liquid-Phase Exfoliation of Layered Perovskite-like Titanates $H LnTiO_4$ and $H_2Ln_2Ti_3O_{10}$ (Ln = La, Nd) into Nanosheets. *Nanomaterials* **2023**, *13*, 3052. [[CrossRef](#)] [[PubMed](#)]
63. Kurnosenko, S.A.; Silyukov, O.I.; Rodionov, I.A.; minich, I.A.; Zvereva, I.A. Pristine and Reassembled Nanosheets of Layered Perovskite-like Titanates $H LnTiO_4$ and $H_2Ln_2Ti_3O_{10}$ (Ln = La, Nd) as Photocatalysts for Hydrogen Evolution. *Solids* **2025**, *6*, 16. [[CrossRef](#)]
64. Makuła, P.; Pacia, M.; Macyk, W. How To Correctly Determine the Band Gap Energy of Modified Semiconductor Photocatalysts Based on UV-Vis Spectra. *J. Phys. Chem. Lett.* **2018**, *9*, 6814–6817. [[CrossRef](#)]
65. Teng, J.; Li, F.; Li, T.; Huttula, M.; Cao, W. Enhanced Visible Light-Driven Hydrogen Evolution in Non-Precious Metal $Ni_2P/CdIn_2S_4$ S-Type Heterojunction via Rapid Interfacial Charge Transfer. *Mater. Today Adv.* **2024**, *22*, 100503. [[CrossRef](#)]
66. Wang, H.; Xu, X.; Labidi, A.; Ren, H.; Allam, A.A.; Rady, A.; Huang, Y.; Wei, S.; Padervand, M.; Ghasemi, S.; et al. Cyano/Hydroxyl Groups Co-Functionalized $g-C_3N_4$ for Photocatalytic NO Removal: A Synergistic Strategy towards Inhibition of Toxic Intermediate NO_2 . *Catalysts* **2023**, *13*, 1433. [[CrossRef](#)]
67. Tang, M.; Li, X.; Deng, F.; Han, L.; Xie, Y.; Huang, J.; Chen, Z.; Feng, Z.; Zhou, Y. $BiPO_4/Ov-BiOBr$ High-Low Junctions for Efficient Visible Light Photocatalytic Performance for Tetracycline Degradation and H_2O_2 Production. *Catalysts* **2023**, *13*, 634. [[CrossRef](#)]

68. Li, Y.; Natakorn, S.; Chen, Y.; Safar, M.; Cunningham, M.; Tian, J.; Li, D.D.U. Investigations on Average Fluorescence Lifetimes for Visualizing Multi-Exponential Decays. *Front. Phys.* **2020**, *8*, 576862. [[CrossRef](#)]
69. Shannon, R.D. Revised Effective Ionic Radii in Halides and Chalcogenides. *Acta Crystallogr.* **1976**, *A32*, 751–767. [[CrossRef](#)]
70. Toda, K.; Kameo, Y.; Fujimoto, M.; Sato, M. Crystal Structure and Ionic Conductivity of a Layered Perovskite, $\text{Na}_2\text{La}_2\text{Ti}_3\text{O}_{10}$. *J. Ceram. Soc. Jpn.* **1994**, *102*, 737–741. [[CrossRef](#)]
71. Kim, H.J.; Byeon, S.H.; Yun, H. Raman Spectra of the Solid-Solution between $\text{Rb}_2\text{La}_2\text{Ti}_3\text{O}_{10}$ and $\text{RbCa}_2\text{Nb}_3\text{O}_{10}$. *Bull. Korean Chem. Soc.* **2001**, *22*, 298–302.
72. Zvereva, I.A.; Silyukov, O.I.; Chislov, M.V. Ion-Exchange Reactions in the Structure of Perovskite-like Layered Oxides: I. Protonation of NaNdTiO_4 Complex Oxide. *Russ. J. Gen. Chem.* **2011**, *81*, 1434–1441. [[CrossRef](#)]
73. Nirala, G.; Yadav, D.; Upadhyay, S. Thermally Activated Polaron Tunnelling Conduction Mechanism in Sr_2MnO_4 Synthesized by Quenching in Ambient Atmosphere. *Phys. Scr.* **2021**, *96*, 045811. [[CrossRef](#)]
74. Díaz-Verde, D.; Illán-Gómez, M.J. Enhancing the Performance of Ba_xMnO_3 ($x = 1, 0.9, 0.8$ and 0.7) Perovskites as Catalysts for CO Oxidation by Decreasing the Ba Content. *Nanomaterials* **2024**, *14*, 1334. [[CrossRef](#)] [[PubMed](#)]
75. Natile, M.M.; Galenda, A.; Glisenti, A. From La_2O_3 To LaCoO_3 : XPS Analysis. *Surf. Sci. Spectra* **2008**, *15*, 1–13. [[CrossRef](#)]
76. Liu, L.; Guo, D.; Cui, W.; Hu, J.; Liang, Y. Photocatalytic Hydrogen Evolution from the Splitting of Water over $\text{Cd}_{1-x}\text{Zn}_x\text{S}/\text{K}_2\text{La}_2\text{Ti}_3\text{O}_{10}$ Composites under Visible Light Irradiation. *J. Wuhan Univ. Technol. Mater. Sci. Ed.* **2015**, *30*, 928–934. [[CrossRef](#)]
77. Kurnosenko, S.A.; Silyukov, O.I.; Zvereva, I.A. Preparation of Porous Particles of Layered Perovskite-Like Titanate HLaTiO_4 . *Glas. Phys. Chem.* **2020**, *46*, 272–276. [[CrossRef](#)]
78. Zhang, W.; Chu, Y.; Wang, C.; Zhao, Y.; Chu, W.; Zhao, J. Enhancing Photocatalytic Hydrogen Production Efficiency in All-Inorganic Lead-Free Double Perovskites via Silver Doping-Induced Efficient Separation of Photogenerated Carriers. *Sep. Purif. Technol.* **2025**, *357*, 130111. [[CrossRef](#)]
79. Jiamprasertboon, A.; Promkamat, P.; Kafizas, A.; Eknapakul, T.; Kongpatpanich, K.; Sailuam, W.; Siritanon, T.; Yoskamtorn, T.; Sotho, K.; Cheacharoen, R.; et al. Porous Nanosheets and Excellent Charge Carrier Dynamics in Ag^+ -Doped $\text{Na}_{0.5}\text{Bi}_{2.5}\text{Nb}_2\text{O}_9$ Aurivillius-Phase Layered Perovskite for Enhanced Visible-Light Photocatalytic Activity. *Chem.-Asian J.* **2025**, e202500151. [[CrossRef](#)]
80. Al-Azri, Z.H.N.; Chen, W.T.; Chan, A.; Jovic, V.; Ina, T.; Idriss, H.; Waterhouse, G.I.N. The Roles of Metal Co-Catalysts and Reaction Media in Photocatalytic Hydrogen Production: Performance Evaluation of M/TiO_2 Photocatalysts ($\text{M} = \text{Pd}, \text{Pt}, \text{Au}$) in Different Alcohol-Water Mixtures. *J. Catal.* **2015**, *329*, 355–367. [[CrossRef](#)]
81. Hwang, D.W.; Kim, H.G.; Jang, J.S.; Bae, S.W.; Ji, S.M.; Lee, J.S. Photocatalytic Decomposition of Water-Methanol Solution over Metal-Doped Layered Perovskites under Visible Light Irradiation. *Catal. Today* **2004**, *93–95*, 845–850. [[CrossRef](#)]
82. Chen, W.; Dong, X.F.; Chen, Z.S.; Chen, S.Z.; Lin, W.M. Effect of Fe^{3+} Doping on Photocatalytic Activity of $\text{K}_2\text{La}_2\text{Ti}_3\text{O}_{10}$ for Water Decomposition to Hydrogen under Visible Light. *Acta Phys.-Chim. Sin.* **2009**, *25*, 1107–1110. [[CrossRef](#)]
83. Hu, Y.; Shi, J.; Guo, L. Enhanced Photocatalytic Hydrogen Production Activity of Chromium Doped Lead Niobate under Visible-Light Irradiation. *Appl. Catal. A Gen.* **2013**, *468*, 403–409. [[CrossRef](#)]
84. Luxová, J.; Dohnalová, Ž.; Šulcová, P.; Reinders, N. Mn-Doped SrTiO_3 Perovskite: Synthesis and Characterisation of a Visible Light-Active Semiconductor. *Mater. Sci. Eng. B* **2025**, *313*, 117889. [[CrossRef](#)]
85. Périllat-Merceroz, C.; Roussel, P.; Huvé, M.; Capoen, E.; Rosini, S.; Gélin, P.; Vannier, R.N.; Gauthier, G.H. Pure and Mn-Doped $\text{La}_4\text{SrTi}_5\text{O}_{17}$ Layered Perovskite as Potential Solid Oxide Fuel Cell Material: Structure and Anodic Performance. *J. Power Sources* **2015**, *274*, 806–815. [[CrossRef](#)]
86. Fang, S.; Hu, Y.H. Thermo-Photo Catalysis: A Whole Greater than the Sum of Its Parts. *Chem. Sci.* **2022**, *51*, 3609–3647. [[CrossRef](#)]
87. Nair, V.; Muñoz-Batista, M.J.; Fernández-García, M.; Luque, R.; Colmenares, J.C. Thermo-Photocatalysis: Environmental and Energy Applications. *ChemSusChem* **2019**, *12*, 2098–2116. [[CrossRef](#)]
88. Fang, J.; Wang, D.; Xu, H.; Sun, F.; Fan, Y.; Chen, R.; Liu, Q. Unleashing Solar Energy's Full Potential: Synergistic Thermo-Photo Catalysis for Enhanced Hydrogen Production with Metal-Free Carbon Nitrides. *Energy Convers. Manag.* **2024**, *300*, 117995. [[CrossRef](#)]
89. Ma, R.; Sun, J.; Li, D.H.; Wei, J.J. Review of Synergistic Photo-Thermo-Catalysis: Mechanisms, Materials and Applications. *Int. J. Hydrogen Energy* **2020**, *45*, 30288–30324. [[CrossRef](#)]

Disclaimer/Publisher's Note: The statements, opinions and data contained in all publications are solely those of the individual author(s) and contributor(s) and not of MDPI and/or the editor(s). MDPI and/or the editor(s) disclaim responsibility for any injury to people or property resulting from any ideas, methods, instructions or products referred to in the content.